Stability of Pd_3Pb Nanocubes during Electrocatalytic Ethanol Oxidation

Xiaoting Yu [a,b], Zhishan Luo [c,d], Ting Zhang [a,e], Pengyi Tang [e], Junshan Li [a,b], Xiang Wang [a,b], Jordi Llorca [f], Jordi Arbiol [e,g], Junfeng Liu [h,*], Andreu Cabot [a,g,*]

a Catalonia Institute for Energy Research - IREC, Sant Adrià de Besòs, 08930 Barcelona, Spain

b Department of Electronic and Biomedical Engineering, Universitat de Barcelona, 08028 Barcelona, Spain

c Department of Chemistry, Southern University of Science and Technology (SUSTech),518055 Shenzhen, Guangdong, P. R. China

d SUSTech Academy for Advanced Interdisciplinary Studies, Southern University of Science and Technology (SUSTech), 518055 Shenzhen, Guangdong, P. R. China

e Catalan Institute of Nanoscience and Nanotechnology (ICN2), CSIC and BIST, Campus UAB, Bellaterra, 08193 Barcelona, Spain

f Institute of Energy Technologies, Department of Chemical Engineering and Barcelona Research Center in Multiscale Science and Engineering, Universitat Politècnica de Catalunya, EEBE, 08019 Barcelona, Spain

g ICREA, Pg. Lluís Companys 23, 08010 Barcelona, Spain

h Institute for Energy Research, School of Chemistry and Chemical Engineering, Jiangsu University, 212013 Zhenjiang, P.R.China

ABSTRACT

Intermetallic Pd_3Pb nanocrystals with controlled size and cubic geometry exposing (100) facets are synthesized by reacting palladium(II) acetylacetonate with lead(II) oxide in the presence of oleylamine, oleic acid and trioctylphosphine. The obtained Pd_3Pb nanocrystals are supported on carbon black and tested as electrocatalysts for ethanol oxidation in alkaline media. We observe the ethanol oxidation activity and stability to be size-dependent. 10 nm Pd_3Pb nanocrystals display the highest initial current densities, but after 1000 cycles, the current density of smaller nanocrystals becomes much larger. All the catalysts exhibit a pronounced current decay during the first 500 s of continuous operation, which is associated to the accumulation of strongly adsorbed reaction intermediates blocking reaction sites. These adsorbed species can be removed by cycling the catalysts or maintaining them at slightly higher potentials for a short period of time to oxidize and later reduce the Pd surface. Such simple cleaning processes, that can be performed

during operation breaks without cell disassembly, is sufficient to effectively remove the poisoning species adsorbed on the surface and recover the electrocatalytic activity.

Keywords: palladium-based, intermetallic, ethanol oxidation, stability

1. INTRODUCTION

Direct alcohol fuel cells are a particularly interesting energy technology to power mobile applications.[1,2] Being liquid at ambient temperature, low-molecular weight alcohols are easy to handle and store, and provide high energy densities, comparable to that of gasoline.[3] While the simplest alcohol fuel, methanol, has been the most extensively investigated, disadvantages such as membrane permeation, high volatility and toxicity are limiting its deployment.[1] Alternatively, ethanol mitigates the methanol drawbacks offering comparable electrochemical activity and energy density, with the additional advantage of potential biosourcing. Thus the research for more active and cost-effective ethanol oxidation catalysts is a worth endeavor.

Pd is an excellent catalyst for the oxidation of hydrogen and liquid fuels,[4] and provides the best performances in alkaline-type direct ethanol fuel cells (DEFCs).[5-7] In terms of surface facets, Pd nanocrystals (NCs) with cubic geometry and offering (100) facets display electrocatalytic performance above that of octahedrons with (111) facets and rhombic dodecahedrons with (110) facets.[8] However, the catalytic activity, selectivity, and especially stability of pure Pd catalysts require further optimization for cost-effective commercialization.[9]

Alloying Pd with additional elements is a common strategy to further improve electrocatalytic performances.[10,11] Adatoms are commonly considered to improve electrocatalytic characteristics through three basic mechanisms: i) Electronic effect, when adatoms alter the electronic nature of active atoms; ii) Steric effect, when the adatom blocks neighboring catalyst site, preventing formation of strongly-bound poison intermediates; iii) Bifunctional effect, when adatoms directly participate in the catalytic oxidation of the fuel.[12] Among the different elements able to promote Pd electrocatalytic performance, e.g. Pd_2Sn,[13,14] PdCu,[15,16] Pd_2Ru,[17] PdAu,[18] and PdNi,[19,20] alloying Pd with Pb results in the highest EOR activity improvement. Pb enhancement has been explained through a combination of a bifunctional mechanism and an electronic effect. In the first direction, Pb plays a key role on the oxidation of absorbed intermediates, which is the limiting step in EOR.[21-25] In particular, the oxidation and stripping of intermediate acetyl, which strongly bind to the catalyst surface, is regarded as the rate- determining step of the ethanol electrooxidation catalyzed by Pd in alkaline media.[26] Pb can activate the water at lower potentials than Pd to oxidize this adsorbed intermediate and liberate Pd active sites. Through the same mechanism, the addition of Pb can improve poisoning tolerance and even help to cleave the C-C bond,[27] overall improving both activity and stability of the catalyst. Additionally, according to the d-band model by Nørskov,[28,29] the introduction of Pb atoms into

Pd can also promote ethanol oxidation by changing the electronic properties of Pd.[25] When Pd with small lattice constant (3.89 Å) is alloyed with Pb with large lattice constant (4.93 Å), the d-band center of Pd shifts up, which improves the ethanol adsorption ability on the surface of Pd_3Pb catalysts.

While most of these fundamental studies have been carried out on well-defined surfaces, real catalysts display a much wider phenomenology. Catalytic performance depends not only on the overall composition of the catalyst, but also on the catalyst crystal domain size and shape, the surface distribution of the elements and their reorganization during operation/cycling. In this regard, Pd_3Pb NCs with a large variety of sizes and shapes, including flower-like,[21] nanowire,[30] nanocubes,[31] nanoplates,[32] and tripods[33] have been reported for oxygen reduction[32-34] and oxidation of formic acid[35,36] and alcohols,[25,37] but showing a large variety of results.

Herein, intermetallic Pd_3Pb NCs with cubic shape and size in the range from 6 nm to 10 nm were synthesized and supported on carbon black. The obtained catalysts were tested toward ethanol oxidation in alkaline media to compare the influence of NC parameters on the EOR electrocatalytic activity and stability.

2. EXPERIMENTAL SECTION

Chemicals. Palladium(II) acetylacetonate ($Pd(acac)_2$, 99%), lead(II) oxide (PbO, 99%), lead(IV) acetate ($Pb(OAc)_4$, 99%), oleylamine (OAm, 80%), oleic acid (OAc, 90%), trioctylphosphine (TOP, 90%), methylamine hydrochloride (MAC, 98%), potassium hydroxide (KOH, 85%), Nafion (5 wt%) were all purchased from Sigma-Aldrich. Hexane, ethanol (EtOH) and acetone were technical grade, obtained from other company and used without further purification.

6 nm Pd_3Pb NCs. 46 mg $Pd(acac)_2$, 11 mg PbO, 1 mL OAc and 10 mL OAm were mixed in a 25 mL three-neck flask connected to Schlenk line with magnetic stirring. 1 mL TOP was injected into the mixture under argon flow. The reaction mixture was purged with argon at 100 °C for 1h. Then the reaction temperature was increased to 200 °C in 10 min and kept at 200 °C for 1 h before cooling down to ambient temperature. The product was collected by centrifugation at 4000 rpm and purified by 3 cycles of dispersion/precipitation with hexane and acetone. NCs were dispersed in hexane until posterior application.

8 nm Pd_3Pb NCs. 46 mg $Pd(acac)_2$, 11 mg PbO, 34 mg MAC, 1 mL OAc and 10 mL OAm were mixed in a 25 mL three-neck flask connected to Schlenk line with magnetic stirring. 1 mL TOP was injected into the mixture under argon flow. The heating and purification steps were the same as for the synthesis of 6 nm Pd_3Pb NCs.

10 nm Pd_3Pb NCs. 46 mg $Pd(acac)_2$, 22 mg $Pb(OAc)_4$, 34 mg MAC, 1 mL OAc and 10 mL OLA were mixed in a 25 mL three-neck flask connected to Schlenk line with magnetic stirring. 1 mL TOP was injected into the mixture under argon flow. The reaction mixture was purged with argon at 100 °C for 1h. Then the reaction temperature was increased to 300 °C in 15 min and kept at 300 °C for 1h before cooling down to ambient temperature. The heating and purification steps were the same as for the synthesis of 6 nm Pd_3Pb NCs.

Carbon supported Pd_3Pb catalysts. Carbon-supported Pd_3Pb catalysts were prepared following a reported method.[38] 5 mg of Pd_3Pb NCs dispersed in 5 mL of hexane were mixed with 5 mg of Vulcan XC-72 carbon dispersed in EtOH. The mixture was sonicated for 1 h to support the Pd_3Pb NCs on the carbon. Then, carbon-supported Pd_3Pb NCs (Pd_3Pb/C) were collected by centrifugation and dispersed in a mixture of 10 mL EtOH and 1 mL acetic acid by sonication for 30 min. Pd_3Pb/C was washed with EtOH and dried naturally under ambient condition before annealed at 250 °C in argon atmosphere for 1h. The final product was dispersed in isopropanol containing 5% Nafion to make the catalyst ink. The concentration of Pd_3Pb in the catalyst was 1 mg/mL (2 mg of Pd_3Pb/C dispersed in 1 mL isopropanol with 5 μl 5% Nafion).

Electrochemical measurements. Electrochemical measurements were conducted with a BioLogic electrochemical workstation using a three-neck-type cell at room temperature. A Pt gauze was used as counter electrode and Hg/HgO (1 M KOH) as reference electrodes. The working electrode was a 5 mm diameter glassy carbon (GC) electrode with 3 μL of drop-casted catalyst ink. Cyclic voltammetry (CV) curves were recorded at a scan rate of 50 mV s^{-1} in argon-saturated 0.5 M KOH or 0.5 M KOH and 0.5 M ethanol

aqueous solutions. Chronoamperometry (CA) measurements were conducted at potential of -0.1 V vs. Hg/HgO for 7200 s in 0.5 M KOH + 0.5 M ethanol aqueous solution for stability evaluation.

Structural and Chemical Characterization. Size and shape of the Pd_3Pb NCs were characterized by transmission electron microscopy (TEM) using a ZEISS LIBRA 120, operating at 120 kV. High-resolution TEM (HRTEM) studies were conducted using a field emission gun FEI Tecnai F20 microscope at 200 kV with a point-to-point resolution of 0.19 nm. Scanning electron microscopy (SEM) analyses were carried out in a ZEISS Auriga microscope with an energy dispersive X-ray spectroscopy (EDS) detector operating at 20 kV to assess composition. Powder X-ray diffraction (XRD) patterns were collected directly from the as-synthesized NPs dropped on Si (501) substrates on a Bruker AXS D8 Advance X-ray diffractometer with Ni-filtered (2 μm thickness) Cu Kα radiation (λ = 1.5406 Å) operating at 40 kV and 40 mA. A LynxEye linear position-sensitive detector was used in reflection geometry.

3. RESULTS AND DISCUSSION

3.1. Structural and chemical characterization of Pd_3Pb NCs

Figure 1 displays TEM micrographs of the NCs obtained from the above-detailed procedure. The Pb precursor and the amount of MAC were adjusted to produce NCs with different sizes (see experimental section for details, Figure S1). HRTEM analysis showed the NCs to have a crystallographic structure compatible with that of cubic Pd_3Pb, [Pm-3m]-space group 221, and to be strongly faceted in the [100] directions (Figure 1d). XRD analysis confirmed the cubic Pd_3Pb intermetallic structure (JCPDS 01-089-2062, Figure 1e) and displayed the ratio of peak intensities $I_{(200)}/I_{(111)}$ and thus the [100] faceting to increase with the NC size. EELS chemical composition maps demonstrated a homogeneous distribution of the two elements within each NC (Figure 1f) with a ratio Pd/Pb≈3, which matched well with results obtained from HRTEM, XRD and EDS analyses (Figure S2).

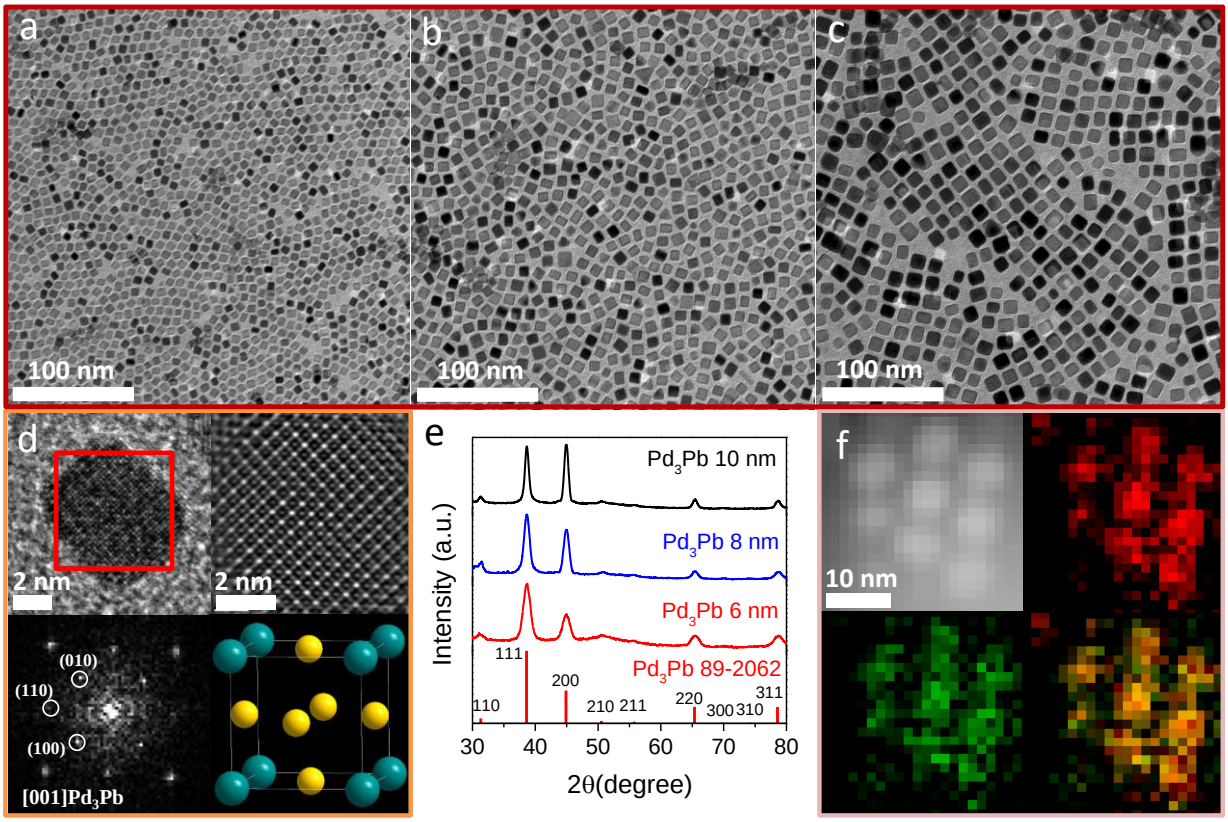

Figure 1. (a-c) TEM micrographs of 6 nm (a), 8 nm (b) and 10 nm Pd_3Pb NCs (c). (d) HRTEM, IFFT image, FFT spectrum after filtering by spot mask, and crystallographic unit cell (yellow for Pd and blue for Pb) of a 6 nm Pd_3Pb NC. HRTEM analysis showed this NC to have a lattice parameter a=b=c=0.4035 nm and α=β=γ=90° as visualized along the [001] direction. (e) XRD patterns of 6 nm, 8 nm and 10 nm Pd_3Pb NCs. (f) ADF-STEM image and EELS composition maps for Pd (red), Pb (green) and Pd-Pb of 6 nm Pd_3Pb NCs.

OAm, OAc and TOP were all necessary components of the precursor reaction mixture to produce highly faceted cubic Pd_3Pb NCs. OAm played two roles, as coordinating solvent forming Pd-OAm complexes, and as mild reducing agent. OAc also played two roles, dissolving PbO to form Pb oleate and directing the shape of the growing NCs by selective surface binding.[39-41] When no OAc was added in the precursor reaction mixture, NCs with irregular geometries and large size distributions were produced (Figure S3a). With the addition of small amounts of OAc, OAc/OAm=0.1, Pd_3Pb NCs with uniform cubic shapes were produced (Figure 1a). However, an excess of OAc, OAc/OAm≥0.2, resulted in spherical Pd_3Pb NCs (Figure S3c).

Without TOP, the Pd-OAm complex decomposed at a lower temperature, ca. 100 °C,[42] forming elemental Pd NPs, i.e. with no Pb alloying. TOP is known to strongly coordinate with Pd to form a Pd-TOP complex.[43] The decomposition of this Pd complex, which is more stable than Pd-OAm, took place at higher temperatures, 200 °C, facilitating the simultaneous reduction of Pd and Pb precursors to form intermetallic Pd_3Pb NCs. Thus, a large excess of TOP, TOP/Pd=15, was introduced in all batches. Besides playing a fundamental role in the control of the NC composition, TOP was also able to direct the NC shape. When larger amounts of TOP were added, instead of cubic NCs, nanoplates/nanorods were grown (Figures S3e and S3f).

Finally, the introduction of MAC and the replacement of PbO by $Pb(OAc)_4$ resulted in larger NCs (Figures 1b,c). We hypothesize this effect to be associated to an increase of the precursor stability in the reaction mixture and a related reduction of the number of nucleation events [44,45] The PbO-MAC system reacted at 200 °C, while the $Pb(OAc)_4$-MAC system required higher temperatures, up to 260 °C, to form Pd_3Pb NCs.

Figure 2a depicted the Pd 3d XPS spectrum of Pd_3Pb NCs, displaying the Pd $3d_{5/2}$ peak at 335.3 eV, i.e. shifted around 0.4 V with respect to Pd^0 (334.9 eV).[46] This binding energy shift was consistent with the introduction of more electronegative Pb that effectively modified the electronic structure of Pd.[31] A second minor component, accounting for 10% of the Pd observed, was associated to Pd^{2+}. This component was related to the binding of surface Pd with surfactant molecules and potentially to a slight surface oxidation of the NCs during manipulation and transportation before XPS measurements.

In the Pb 4f XPS spectrum three 4f doublets were identified, corresponding to three Pb chemical states (Figure 2b). The main peaks at 141.6 eV ($4f_{5/2}$) and 136.7 eV Pb ($4f_{7/2}$) were associated to Pb^0, although were shifted -0.2 eV with respect to the reference value for elemental Pb $4f_{7/2}$ (136.9 eV),[46] consistently with the electronic interaction between Pd and Pb atoms within the Pb_3Pb alloy. A second component was located at 143.0 eV ($4f_{5/2}$) and 138.1 eV ($4f_{7/2}$), and it was assigned to an oxidized Pb state, Pb^{n+}. A third component appeared at even higher binding energies, 139.1 eV ($4f_{7/2}$) and 144.0 eV ($4f_{5/2}$), and it was associated with a Pb^{2+} chemical state. The oxidized Pb components, which we will generally refer to as Pb^{x+}, were associated to the binding of Pb with oleic acid molecules on the NC surface and to a slight surface oxidation of the NCs during handling and transportation. The ratio Pb^0/Pb^{x+} was 1.55. *i.e.* 40% of the Pb at the 2-3 nm-thick outer layer of the Pd_3Pb NCs was oxidized. This percentage was significantly higher than that of Pd. Besides,

the Pd/Pb surface ratio obtained by XPS was 1.19, much lower than the stoichiometric values deduced from EDS, XRD and HRTEM analyses. These results indicated a segregation of Pb atoms to the NC surface during the NC synthesis. This radial gradient of Pb may be also in part driven by oxidation during manipulation and storage in ambient conditions, due to the lower oxidation potential of Pb when compared with Pd.

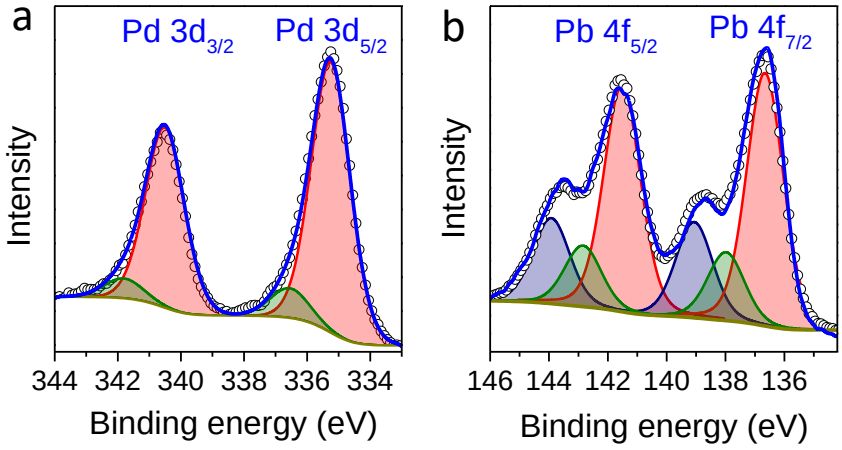

Figure 2. High resolution XPS spectra of 6 nm Pd_3Pb NCs in the regions (a) Pd 3d and (b) Pb 4f.

3.2. CV analysis

Pd_3Pb-based electrocatalysts were prepared by mixing colloidal Pd_3Pb NCs with carbon black, 1:1 wt%. Initial CV analyses were carried out at a sweep rate of 50 mV s^{-1} with an argon-saturated 0.5 M KOH solution. Figure 3a depicts the CV curves recorded for Pd_3Pb/C catalysts with different NC sizes and for a commercial Pd/C catalyst tested as a reference. The same total amount of NCs was used to prepare each of the tested electrodes, which translated in significantly lower amounts of Pd on the Pd_3Pb/C catalysts than on the reference Pd/C.

The current density peaks in the region between -0.6 V and -0.8 V vs. Hg/HgO were attributed to the adsorption (cathodic scan) and desorption (anodic scan) of hydrogen. The current density increase measured at ca. -0.2 V vs. Hg/HgO in the anodic scan is attributed to the formation of palladium oxide on the NC surface. Subsequently, a PdO reduction peak appeared at about -0.2 V vs. Hg/HgO during the negative scans.

Compared with Pd/C, Pd_3Pb/C catalysts displayed less obvious peaks associated to hydrogen desorption and adsorption, owing to the lower amount of Pd on their surface. On the other hand, the intensity of the Pd oxide reduction peak clearly increased with the addition of Pb and when increasing the NC size. Besides, the maximum of this peak was shifted toward higher potentials on Pd_3Pb/C catalysts compared to Pd/C. The

distinct anodic and cathodic characteristics of Pd_3Pb- and Pd-based catalysts were related to their different electronic structure involving partial electron donation from Pd to Pb sites, consistent with XPS results.[47]

The electrochemically active surface area (ECSA) of the catalysts was estimated from the coulombic charge for the reduction of PdO, i.e. from the area over the voltammetry curve in the PdO reduction peak region[14]:

$$\mathrm{ECSA} = \frac{\mathrm{Q}\,(\mu C \cdot cm^{-2})}{Q_{PdO}(\mu C \cdot cm_{Pd}^{-2}) \times Pd_{loading}(mg \cdot cm^{-2}) \times 10} \qquad (1)$$

where Q_{PdO} = 405 µC cm^{-2} was the charge value given for the reduction of a PdO monolayer, the coulombic charge Q was calculated by integrating the area of the PdO reduction peak, and $Pd_{loading}$ was the Pd mass on the working electrode. The calculated ESCA values for 10 nm Pd_3Pb/C (33.6 m^2 g^{-1}) was larger than that of 8 nm (20.2 m^2 g^{-1}) and 6 nm (19.2 m^2 g^{-1}). Besides, the ESCA was significantly larger for all Pd_3Pb/C catalysts compared with Pd/C (14.9 m^2 g^{-1}). ESCA increased during the first cycles for Pd_3Pb/C, but not for commercial Pd/C catalyst. This ESCA increase on Pd_3Pb/C may be related to a reorganization of the surface composition and potentially to a stripping of remaining surface ligands.

After 30 CV cycles, the ECSA values obtained from commercial Pd/C, and for 6 nm, 8 nm and 10 nm Pd_3Pb/C catalysts were 14.9 m^2 g^{-1}, 19.2 m^2 g^{-1}, 20.2 m^2 g^{-1}, and 33.6 m^2 g^{-1}, respectively. The Pd utilization effectiveness was estimated considering that the active surface area for full utilization of 1 g of Pd would be 448 m^2. Thus, the Pd utilization efficiencies of commercial Pd/C, and for 6 nm, 8 nm and 10 nm Pd_3Pb/C catalysts were 3.3 %, 4.3 %, 4.5 %, and 7.5 %, respectively.

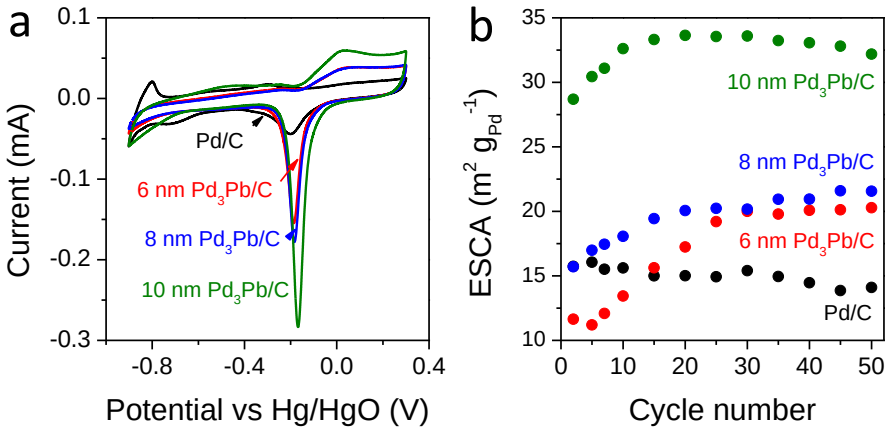

Figure 3. (a) CV curves of 6 nm, 8 nm, 10 nm Pd_3Pb/C and Pd/C catalysts. (b) ESCA values of 6 nm, 8 nm, 10 nm Pd_3Pb/C and Pd/C catalysts at different CV cycles.

3.3. EOR activity, CV analysis

The electrocatalytic activity of Pd_3Pb-based catalysts towards EOR was investigated by CV in a solution containing 0.5 M KOH and 0.5 M EtOH. Figure 3b displays the CV curves of Pd_3Pb/C and Pd/C catalysts after 30 cycles at a sweep rate of 50 mV s^{-1}. In the presence of EtOH, hydrogen absorption-desorption peaks

were suppressed due to the dominant adsorption of EtOH in the low-potential region. The positive scan peak related to the oxidation of freshly adsorbed alcohol started at -0.6 V and reached its maximum at -0.1 V. At higher voltages, the catalytic activity decreased due to the progressive oxidation of the Pd surface. The oxidation peak in the cathodic scan, associated with the oxidation of freshly adsorbed EtOH and of unreacted species adsorbed before or after Pd–O blocking,[48] was triggered by the reduction of the oxide layer grown in the preceding anodic scan.[49] The peak current densities of Pd_3Pb/C catalysts were much higher than those of Pd/C, and the onset potential for EtOH oxidation of Pd_3Pb/C catalysts was more negative than for Pd/C, what suggested a more favorable EOR on the surface of Pd_3Pb/C catalysts than on Pd/C.

Figure 4c exhibits the forward oxidation peak current density for EOR as a function of cyclic scan number. During the first cycles the forward peak current density increased to later decrease gradually with the continued scanning. Such a general trend is often observed in electrocatalytic alcohol oxidation and is generally ascribed to a structural or surface reorganization of the catalyst.[50,51] For Pd/C, the current density decay started at the 50th cycle, dropping from 12.53 to 5.13 mA cm^{-2} after 1000 cycles. A very similar evolution was measured from 10 nm Pd_3Pb/C, with a progressive increase of current density up to approximately the 50^{th} cycle, yet with significantly higher current densities, from 21.82 to 11.72 mA cm^{-2}. 6 nm and 8 nm Pd_3Pb/C catalysts were characterized by a significantly different evolution of the forward peak current density with the cycle number. 6 nm and 8 nm Pd_3Pb/C catalysts displayed a progressive increase of the current density up to the 400^{th}-500^{th} cycle and a quasi-stabilization of the activity at current densities around 20 mA cm^{-2} with additional cycling. Thus, while 10 nm Pd_3Pb/C displayed higher catalytic activity in the initial CV cycles, 6 nm and 8 nm Pd_3Pb/C had much longer durability and higher activities after longer cycling. In terms of mass current density (Figure 4d), after 30 cycles 10 nm Pd_3Pb/C catalyst showed the highest values up to 2.05 A mg^{-1}_{Pd}, while the performance of 6 nm and 8 nm Pd_3Pb/C was slightly lower than that of Pd/C. However, after 1000 cycles, 8 nm Pd_3Pb/C catalyst displayed much larger mass current densities up to 2.05 A mg^{-1}_{Pd}.

The ratio of the maximum intensities measured for the forward and reverse peaks, I_f/I_r, of Pb_3Pb/C catalysts also changed with the cycling number, decreasing for 6 nm Pd_3Pb/C from 1.1 to 0.90, and 8 nm Pd_3Pb, from 1.3 to 0.85, but increasing for 10 nm Pd_3Pb, from 0.82 to 0.93 and increasing very moderately for Pd/C, from 0.90 to 0.91. This ratio is related to the reactivation efficiency, the higher the Ir, the highest the reactivation, which denotes an improvement of the reactivation with cycling for the smallest NCs.[49]

Figure 4f shows the linear region of the Tafel plots obtained from the 30th and 1000th CV curves in the range from −0.5 to -0.2 V vs. Hg/HgO for Pd_3Pb and Pd/C catalysts. From the 30th cycle, the Tafel slopes were: 162 mV dec^{-1} for Pd/C, 156 mV dec^{-1} for 8 nm, 145 mV dec^{-1} for 6 nm and 140 mV dec^{-1} for 10 nm. After 1000 cycles, all the Tafel slopes increased: 197 mV dec^{-1} for Pd/C, 173 mV dec^{-1} for 6 nm, 160 mV dec^{-1} for 8 nm and 157 mV dec^{-1} for 10 nm. All Pd_3Pb/C catalysts displayed lower Tafel slopes and thus faster charge-transfer kinetics than Pd/C. On the other hand, the increase of the Tafel slopes with the scan number revealed a performance decay for all the catalysts, being the 8 nm Pd_3Pb/C catalyst the one showing the best stability.

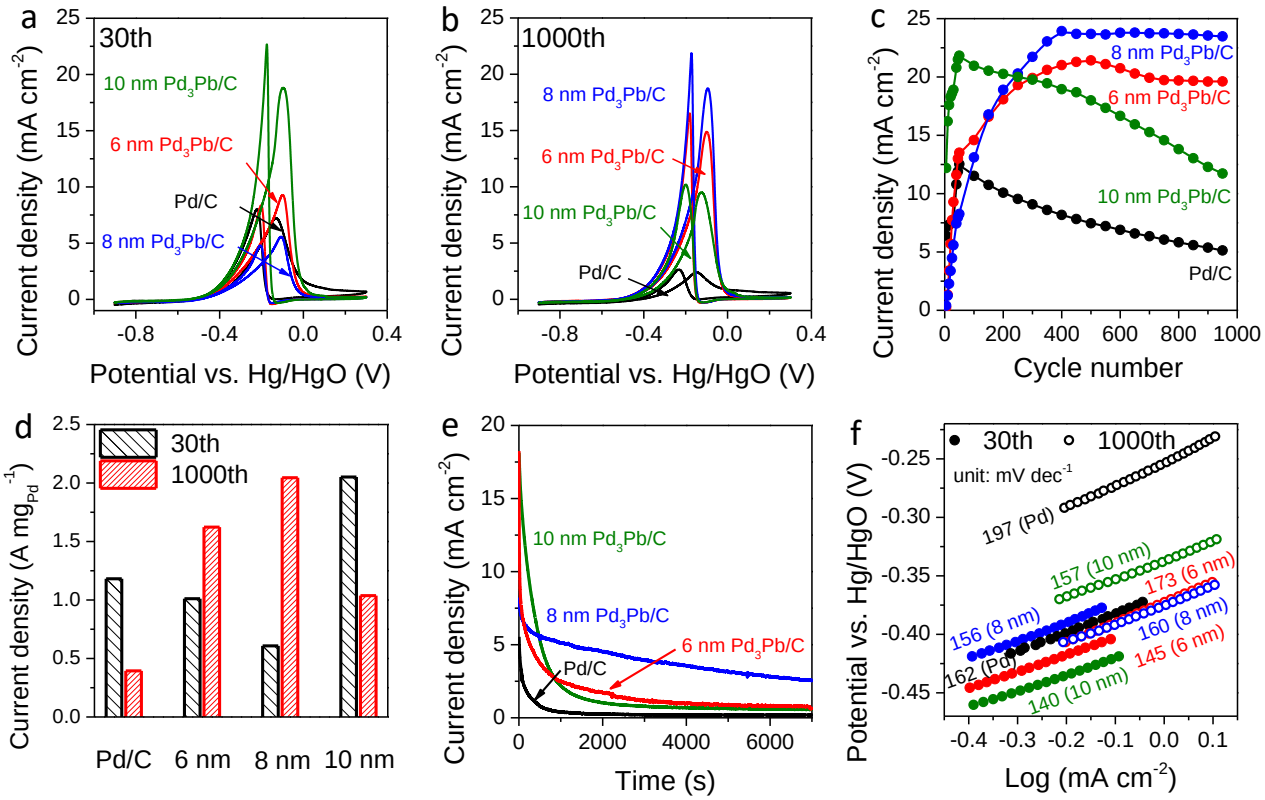

Figure 4. (a) 30th CV curves of 6 nm, 8 nm and 10 nm Pd_3Pb/C and Pd/C catalysts in 0.5 M KOH + 0.5 M EtOH aqueous solution. (b) 1000th CV curves of 6 nm, 8 nm and 10 nm Pd_3Pb/C and Pd/C catalysts in 0.5 M KOH + 0.5 M EtOH aqueous solution. (c) Current density of 6 nm, 8 nm, 10 nm Pd_3Pb/C and Pd/C catalysts in 0.5 M KOH + 0.5 M EtOH solution at potential of -0.1 V vs. Hg/HgO for different CV cycles. (d) Mass peak current density of 6 nm, 8 nm, 10 nm Pd_3Pb/C and Pd/C catalysts in 0.5 M KOH + 0.5 M EtOH aqueous solution from 30th and 1000th CV cycles. (e) CA measurements of 6 nm, 8 nm and 10 nm Pd_3Pb/C and Pd/C catalysts in 0.5 M KOH + 0.5 M EtOH aqueous solution at the potential of −0.1 V vs. Hg/HgO. (f) Tafel plots of 6 nm, 8 nm, 10 nm Pd_3Pb/C and Pd/C catalysts in 0.5 M KOH + 0.5 M EtOH aqueous solution from 30th and 1000th cycles, respectively.

Differences between different particle sizes may be related to several interconnected and simultaneous mechanisms: i) the higher activity of the 10 nm NCs had associated the generation of a higher amount of intermediates that may poison the catalyst surface more rapidly than in less active catalysts; ii) The oxidation and reduction of surface Pd during each scan and the development of channels of electron collection may cause the rearrangement of the catalyst surface.[52] This process may be significantly different in NCs with different sizes; iii) Depending on the NC size, the extend of oxidation and reduction may be significantly different.

3.4. EOR activity, CA analysis

The stability of the catalyst performance was further investigated by CA. Figure 4e displays CA results obtained at -0.1 V vs. Hg/HgO in a 0.5 M KOH + 0.5 M EtOH aqueous solution. All the catalysts exhibited a pronounced current decay during the first 500 s. While all the Pd_3Pb/C catalysts showed enhanced EOR activity and better stability than Pd/C catalyst, 10 nm Pd_3Pb/C catalysts displayed the less abrupt decrease in current densities. The rapid activity decay, characteristic of EOR catalyst including Pd-based catalysts, remains as a major drawback toward the commercialization of DEFCs. Replacing the electrolyte by a fresh solution did not provide a significant increase in current density, demonstrating that the EtOH depletion is not the reason behind the large current density decrease. Instead, we succeeded in reactivating our Pd_3Pb/C and Pd/C catalysts by either cycling few times the applied potential (Figure 5) or by slightly increasing the electrode potential for a short time (Figure S4). Figure 5 displays the current density decay during periods of 1000 s for 10 nm, 8 nm, 6 nm Pd_3Pb/C and Pd/C catalysts. In between these 1000 s periods, 3 CV cycles in the range from -0.9 to 0.3 V vs. Hg/HgO with a rate of 50 mV s^{-1} for a total time of 144 s were applied. 10 nm Pd_3Pb/C catalyst reached the highest current densities after each reactivation. Figure S4 displays the current densities evolution during periods of 1000 s and reactivation by applying a voltage of 0.3 V vs. Hg/HgO for 100 s, i.e. by oxidizing and later reducing the Pd surface.

In alkaline media, EtOH is dehydrogenated into adsorbed acetyl, which is further oxidized to acetate by hydroxide species.[9,26,53] The oxidation of the acetyl to acetic acid by adsorbed hydroxyl is regarded as the rate- determining step, while the stripping of the acetic acid in the form of acetate ions in alkaline solution is very rapid.[9] Acetaldehyde and reaction products such as CH and C may block additional sites, although breaking of the C-C bond is considered to have a minor contribution on the obtained current density.[53,54] It is generally agreed that besides contributing to increase EtOH adsorption by modifying the Pd electronic structure, Pb at the catalyst surface contributes to the EOR by supplying hydroxyl groups.

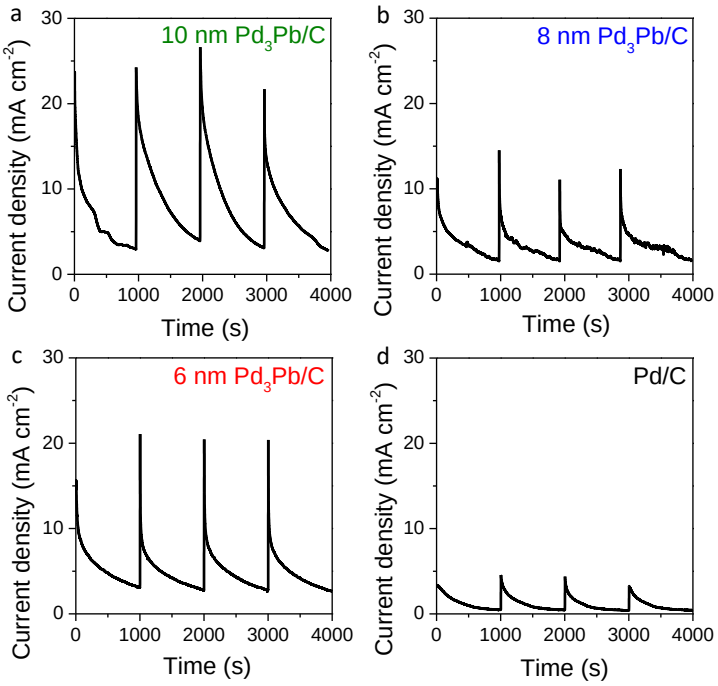

Figure 5. CA curves of 10 nm (a), 8 nm (b), 6 nm (c) Pd_3Pb/C and Pd/C (d) catalysts. Three CV cycles were conducted to reactivate the catalyst every 1000 s.

Cycling contributes to clean the Pd surface through different mechanism. The oxidation of the acetyl to acetate is favored by oxidative potentials.[9] Besides the oxidation of the catalyst surface may contribute to the stripping of adsorbed molecules. In this process, the concentration and surface distribution of Pd and Pb, the overall surface area and exposed facets play an important role. During EOR and during cycling all of these parameters may change. Pd and Pb most probably redistribute within each particle during electrochemical reaction as evidenced below and even within the surface as noted in more detail by Gunji et al.[55] Changes of surface composition modifies the equilibrium coverage of hydroxyl and adsorbed acetyl, thus changing the overall current density.[9] Besides, potential changes of particle geometry modify the exposed facets and thus the exposed distribution of Pb and Pd sites.

3.5. Structural and chemical evolution

HRTEM and HAADF-STEM analysis showed the NCs to maintain a high crystallinity and to conserve the Pd_3Pb intermetallic phase after cycling in 0.5 M KOH and 0.5 M KOH + 0.5 M EtOH aqueous solutions (Figure 6). However, extensive TEM analysis showed the cubic shape of the NCs to be modified with the cycling (Figures S7-13).

XPS analyses of the Pd_3Pb catalyst after cycling in 0.5 M KOH and in 0.5 M KOH + 0.5 M EtOH aqueous solutions showed a notable increase of the surface Pd/Pb atomic ratio, from the initial Pd/Pb=1.3 obtained from Pd_3Pb NCs to Pd/Pb=3.09 of the Pd_3Pb/C catalyst after cycling in a KOH + EtOH aqueous solution

(Figure S5, Table S1). This decrease of the relative Pb surface concentration could be related to a partial dissolution of Pb, a phase segregation, or a redistribution of the elements within each NC.

EDS analysis showed the total Pd/Pb ration to slightly increase after cycling in a 0.5 M KOH + 0.5 M EtOH aqueous solution, from Pd/Pb=3.03 to Pd/Pb=3.42, and after cycling in KOH, Pd/Pb=3.77. This increase must be assigned to a leaching of Pb atoms from the Pd_3Pb alloy. However, the amount of leached Pb, 12 % after a KOH + EtOH aqueous solution, cannot account for the much larger variations obtained on the surface composition. Besides, STEM-EDS analysis of the catalyst after 30 CV cycles in 0.5 M KOH aqueous solution (Figure S6) and EELS analysis after cycling in KOH + EtOH aqueous solutions (Figure 6) displayed no phase segregation, being both elements well distributed within each NC and with the same ratio from particle to particle. These results pointed out at a reorganization of the two elements within the Pd_3Pb NCs during cycling in a KOH + EtOH aqueous solution, involving an outward/inward diffusion of Pd/Pb to equilibrate the stoichiometry of the NCs surface, which is highly Pb-rich in the as-synthesized materials.

Actually, a partial surface reorganization took place already during the catalyst preparation, which may be related with the removal of organic ligands that were preferentially bond to Pb atoms. Additional decrease of the Pb surface concentration was observed during cycling in KOH (Table S1). This decrease was partially correlated with EDS results that showed an important Pb leaching during KOH cycling. However, we believe that a significant part of the elemental restructuration is driven by the oxidation/reduction of Pd. During cycling, only Pd was oxidized and reduced, while surface Pb atoms remained in an oxidized chemical state. In a previous work, we showed how cobalt and copper can reorganize by interfusion during oxidation and reduction processes. During oxidation Co diffuses outward to form a $CuO\text{-}Co_3O_4$ hollow structures, while during reduction Cu diffuses inward to form $Cu@Co_3O_4$ core-shell particles.[56] In the present case we believe a similar effect takes place. The initial NC surface is enriched with Pb due to the larger affinity of this element toward organic ligands and oxygen. Once removed the organics, during cycling Pd diffuses outwards/inwards driven by the oxidation/reduction processes. Since the largest increase of the surface Pd/Pb ratio was obtained after cycling in the presence of EtOH, we need to assume that the higher affinity of Pd to EtOH may also play an important role in the surface restructuration.

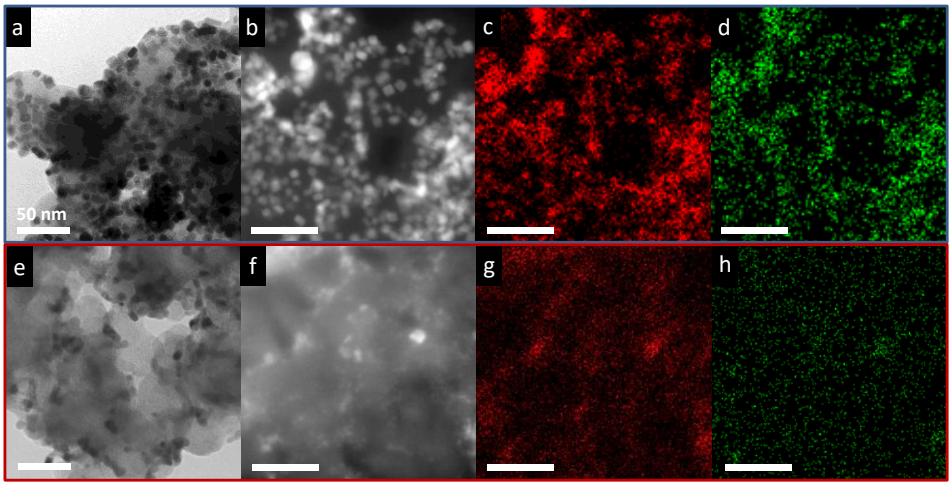

Figure 6. (a) TEM and (b) HAADF-STEM micrographs of 6 nm Pd_3Pb/C catalyst. HAADF-EDS mappings of (c) Pd and (d) Pb from 6 nm Pd_3Pb/C catalyst. (e) TEM and (f) HAADF-STEM micrographs of 6 nm Pd_3Pb/C catalyst after 30 CV cycles in a 0.5 KOH + 0.5 M EtOH aqueous solution. HAADF-EDS mappings of (g) Pd and (h) Pb from 6 nm Pd_3Pb/C catalyst after 30 CV cycles in a 0.5 KOH + 0.5 M EtOH aqueous solution. All scale bars are 50 nm.

4. CONCLUSIONS

In summary, we report a simple approach to produce intermetallic Pd_3Pb NCs with cubic geometry and size in the range from 6 nm to 10 nm. Compared with commercial Pd/C catalyst, Pd_3Pb/C catalysts presented improved EOR electrocatalytic activities. 10 nm Pd_3Pb/C catalyst provided the largest initial current densities, but smaller NCs were able to reach higher current densities after extended cycling. All the catalysts exhibited a pronounced current decay during the first 500 s of continuous EOR operation, which was associated to the accumulation of strongly adsorbed reaction intermediates and the blockage of reaction sites. The catalyst could be reactivated by simple cycling, but this reactivation was also size dependent. Such simple cleaning processes, that can be performed during operation breaks without cell disassembly, was sufficient to effectively remove the poisoning species adsorbed on the surface and recover the electrocatalytic activity. We finally demonstrated that during cycling a major restructuration of the element distribution within the NCs took place, driven by the different affinity of Pb and Pd towards oxygen and possibly ethanol and the electrochemical oxidation/reduction of Pd.

ACKNOWLEDGEMENTS

This work was supported by the European Regional Development Funds and by the Spanish Ministerio de Economía y Competitividad through the project SEHTOP, ENE2016-77798-C4-3-R and VALPEC and subprojects RESOL and ANAPHASE ENE2017-85087-C3. X. Yu thanks the China Scholarship Council for the scholarship support. Authors acknowledge funding from Generalitat de Catalunya 2017 SGR 327 and 2017

SGR 1246. ICN2 acknowledges support from the Severo Ochoa Programme (MINECO, Grant no. SEV-2017-0706) and is funded by the CERCA Programme/Generalitat de Catalunya. J. Llorca is a Serra Húnter Fellow and is grateful to ICREA Academia program and to MINECO/FEDER grant RTI2018-093996-B-C31 and GC 2017 SGR 128. Part of the present work has been performed in the framework of Universitat Autònoma de Barcelona Materials Science PhD program. T. Zhang has received funding from the CSC-UAB PhD scholarship program.

REFERENCES

(1) Lamy, C.; Lima, A.; LeRhun, V.; Delime, F.; Coutanceau, C.; Léger, J. Recent Advances in the Development of Direct Alcohol Fuel Cells (DAFC). *J. Power Sources* **2002**, *105*, 283–296.

(2) Antolini, E. Catalysts for Direct Ethanol Fuel Cells. *J. Power Sources* **2007**, *170*, 1–12.

(3) Lamy, C.; Belgsir, E. M.; Léger, J.-M. Electrocatalytic Oxidation of Aliphatic Alcohols : Application to the Direct Alcohol Fuel Cell (DAFC). *J. Appl. Electrochem.* **2001**, *31*, 799–809.

(4) Chen, A.; Ostrom, C. Palladium-Based Nanomaterials: Synthesis and Electrochemical Applications. *Chem. Rev.* **2015**, *115*, 11999–12044.

(5) Takamura, T.; Minamiyama, K. Anodic Oxidation of Methanol at Palladium Electrode in Alkaline Solution. *J. Electrochem. Soc.* **1965**, *112* (3), 333–335.

(6) Hu, F.; Chen, C.; Wang, Z.; Wei, G.; Kang, P. Mechanistic Study of Ethanol Oxidation on Pd–NiO C Electrocatalyst. *Electrochim. Acta* **2006**, *52*, 1087–1091.

(7) Ma, L.; Chu, D.; Chen, R. Comparison of Ethanol Electro-Oxidation on Pt/C and Pd/C Catalysts in Alkaline Media. *Int. J. Hydrogen Energy* **2012**, *37* (15), 11185–11194.

(8) Ma, X. Y.; Chen, Y.; Wang, H.; Li, Q. X.; Lin, W. F.; Cai, W. Bin. Electrocatalytic Oxidation of Ethanol and Ethylene Glycol on Cubic, Octahedral and Rhombic Dodecahedral Palladium Nanocrystals. *Chem. Commun.* **2018**, *54*, 2562–2565.

(9) Liang, Z. X.; Zhao, T. S.; Xu, J. B.; Zhu, L. D. Mechanism Study of the Ethanol Oxidation Reaction on Palladium in Alkaline Media. *Electrochim. Acta* **2009**, *54* (8), 2203–2208.

(10) Bianchini, C.; Shen, P. K. Palladium-Based Electrocatalysts for Alcohol Oxidation in Half Cells and in Direct Alcohol Fuel Cells. *Chem. Rev.* **2009**, *109*, 4183–4206.

(11) Iqbal, M.; Kaneti, Y. V.; Kim, J.; Yuliarto, B.; Kang, Y.-M.; Bando, Y.; Sugahara, Y.; Yamauch, Y. Chemical Design of Palladium-Based Nanoarchitectures for Catalytic Applications. *Small* **2019**, 1804378.

(12) Sadiki, A.; Vo, P.; Hu, S.; Copenhaver, T. S.; Scudiero, L.; Ha, S.; Haan, J. L. Increased Electrochemical Oxidation Rate of Alcohols in Alkaline Media on Palladium Surfaces Electrochemically Modified by Antimony, Lead, and Tin. *Electrochim. Acta* **2014**, *139*, 302–307.

(13) Luo, Z.; Lu, J.; Flox, C.; Nafria, R.; Genç, A.; Arbiol, J.; Llorca, J.; Ibáñez, M.; Morante, J. R.; Cabot, A. Pd2Sn [010] Nanorods as a Highly Active and Stable Ethanol Oxidation Catalyst. *J. Mater. Chem. A* **2016**, *4*, 16706–16713.

(14) Wang, C.; Wu, Y.; Wang, X.; Zou, L.; Zou, Z.; Yang, H. Low Temperature and Surfactant-Free Synthesis of Pd2Sn Intermetallic Nanoparticles for Ethanol Electro-Oxidation. *Electrochim. Acta* **2016**, *220*, 628–634.

(15) Jiang, K.; Wang, P.; Guo, S.; Zhang, X.; Shen, X.; Lu, G.; Su, D.; Huang, X. Ordered PdCu-Based Nanoparticles as Bifunctional Oxygen-Reduction and Ethanol-Oxidation Electrocatalysts. *Angew. Chem. Int. Ed* **2016**, *55*, 9030–9035.

(16) Zhao, X.; Dai, L.; Qin, Q.; Pei, F.; Hu, C.; Zheng, N. Self-Supported 3D PdCu Alloy Nanosheets as a Bifunctional Catalyst for Electrochemical Reforming of Ethanol. *Small* **2017**, *13*, 1602970.

(17) Guo, J.; Chen, R.; Zhu, F. C.; Sun, S. G.; Villullas, H. M. New Understandings of Ethanol Oxidation Reaction Mechanism on Pd/C and Pd2Ru/C Catalysts in Alkaline Direct Ethanol Fuel Cells. *Appl. Catal. B Environ.* **2018**, *224*, 602–611.

(18) Liu, J.; Zheng, Y.; Hong, Z.; Cai, K.; Zhao, F.; Han, H. Microbial Synthesis of Highly Dispersed PdAu Alloy for Enhanced Electrocatalysis. *Sci. Adv.* **2016**, *2* (9), 1600858.

(19) Chen, Z.; Zhang, J.; Zhang, Y.; Liu, Y.; Han, X.; Zhong, C.; Hu, W.; Deng, Y. NiO-Induced Synthesis of PdNi Bimetallic Hollow Nanocrystals with Enhanced Electrocatalytic Activities toward Ethanol and Formic Acid Oxidation. *Nano Energy* **2017**, *42*, 353–362.

(20) Cai, B.; Wen, D.; Liu, W.; Herrmann, A. K.; Benad, A.; Eychmüller, A. Function-Led Design of Aerogels: Self-Assembly of Alloyed PdNi Hollow Nanospheres for Efficient Electrocatalysis. *Angew. Chem. Int. Ed* **2015**, *54*, 13101–13105.

(21) Jana, R.; Subbarao, U.; Peter, S. C. Ultrafast Synthesis of Flower-like Ordered Pd3Pb Nanocrystals with Superior Electrocatalytic Activities towards Oxidation of Formic Acid and Ethanol. *J. Power Sources* **2016**, *301*, 160–169.

(22) Wu, P.; Huang, Y.; Kang, L.; Wu, M.; Wang, Y. Multisource Synergistic Electrocatalytic Oxidation Effect of Strongly Coupled PdM (M=Sn, Pb)/N-Doped Graphene Nanocomposite on Small Organic Molecules. *Sci. Rep.* **2015**, *5*, 14173.

(23) Wu, P.; Huang, Y.; Zhou, L.; Wang, Y.; Bu, Y.; Yao, J. Nitrogen-Doped Graphene Supported Highly Dispersed Palladium-Lead Nanoparticles for Synergetic Enhancement of Ethanol Electrooxidation in

Alkaline Medium. *Electrochim. Acta* **2015**, *152*, 68–74.
(24) Li, G.; Pickup, P. G. The Promoting Effect of Pb on Carbon Supported Pt and Pt/Ru Catalysts for Electro-Oxidation of Ethanol. *Electrochim. Acta* **2006**, *52*, 1033–1037.
(25) Wang, Y.; Nguyen, T. S.; Liu, X.; Wang, X. Novel Palladium-Lead (Pd-Pb/C) Bimetallic Catalysts for Electrooxidation of Ethanol in Alkaline Media. *J. Power Sources* **2010**, *195*, 2619–2622.
(26) Liang, Z. X.; Zhao, T. S.; Xu, J. B.; Zhu, L. D. Mechanism Study of the Ethanol Oxidation Reaction on Palladium in Alkaline Media. *Electrochim. Acta* **2009**, *54*, 2203–2208.
(27) He, Q.; Shyam, B.; Macounová, K.; Krtil, P.; Ramaker, D.; Mukerjee, S. Dramatically Enhanced Cleavage of the C−C Bond Using an Electrocatalytically Coupled Reaction. *J. Am. Chem. Soc.* **2012**, *134*, 8655–8661.
(28) Nørskov, J. K.; Abild-pedersen, F.; Studt, F.; Bligaard, T. Density Functional Theory in Surface Chemistry and Catalysis. *Proc. Natl. Acad. Sci. U. S. A.* **2011**, *108* (3), 937–943.
(29) Hammer, B.; Norskov, J. K. Why Gold Is the Noblest of All the Metals. *Nature* **1995**, *376* (6537), 238–240.
(30) Shi, Q.; Zhu, C.; Bi, C.; Xia, H.; Engelhard, M. H.; Du, D.; Lin, Y. Intermetallic Pd3Pb Nanowire Networks Boost Ethanol Oxidation and Oxygen Reduction Reactions with Significantly Improved Methanol Tolerance. *J. Mater. Chem. A* **2017**, *5*, 23952–23959.
(31) Zhang, J.; Xu, W.; Xu, L.; Shao, Q.; Huang, X. Concavity Tuning of Intermetallic Pd-Pb Nanocubes for Selective Semihydrogenation Catalysis. *Chem. Mater.* **2018**, *30* (18), 6338–6345.
(32) Wang, K.; Qin, Y.; Lv, F.; Li, M.; Liu, Q.; Lin, F.; Feng, J.; Yang, C.; Gao, P.; Guo, S. Intermetallic Pd3Pb Nanoplates Enhance Oxygen Reduction Catalysis with Excellent Methanol Tolerance. *Small Methods* **2018**, *1700331*, 1700331.
(33) Bu, L.; Shao, Q.; Pi, Y.; Yao, J.; Luo, M.; Lang, J.; Hwang, S.; Xin, H.; Huang, B.; Guo, J.; et al. Coupled S-p-d Exchange in Facet-Controlled Pd3Pb Tripods Enhances Oxygen Reduction Catalysis. *Chem* **2018**, *4* (2), 359–371.
(34) Cui, Z.; Chen, H.; Zhao, M.; Disalvo, F. J. High-Performance Pd3Pb Intermetallic Catalyst for Electrochemical Oxygen Reduction. *Nano Lett.* **2016**, *16* (4), 2560–2566.
(35) Yu, X.; Pickup, P. G. Novel Pd-Pb/C Bimetallic Catalysts for Direct Formic Acid Fuel Cells. *J. Power Sources* **2009**, *192* (2), 279–284.
(36) Li, R.; Hao, H.; Cai, W. Bin; Huang, T.; Yu, A. Preparation of Carbon Supported Pd-Pb Hollow Nanospheres and Their Electrocatalytic Activities for Formic Acid Oxidation. *Electrochem. commun.* **2010**, *12* (7), 901–904.
(37) Bu, L.; Tang, C.; Shao, Q.; Zhu, X.; Huang, X. Three-Dimensional Pd3Pb Nanosheet Assemblies: High-Performance Non-Pt Electrocatalysts for Bifunctional Fuel Cell Reactions. *ACS Catal.* **2018**, *8*, 4569–4575.
(38) Bu, L.; Zhang, N.; Guo, S.; Zhang, X.; Li, J.; Yao, J.; Wu, T.; Lu, G.; Ma, J. Y.; Su, D.; et al. Biaxially Strained PtPb/Pt Core/Shell Nanoplate Boosts Oxygen Reduction Catalysis SI. *Science (80-.).* **2016**, *354* (6318), 1410–1414.
(39) Resa, I.; Moreira, H.; Bresson, B.; Mahler, B.; Dubertret, B.; Aubin, H. Synthesis of Monodisperse Superconducting Lead Nanocrystals. *J. Phys. Chem. C* **2009**, *113*, 7120–7122.
(40) Zhang, D.; Zhai, G.; Zhang, J.; Yuan, L.; Miao, X.; Wang, Y. Growth Orientation and Shape Evolution of Colloidal Lead Selenide Nanocrystals with Different Shapes. *CrystEngComm* **2010**, *12*, 3243–3248.
(41) Zherebetskyy, D.; Scheele, M.; Zhang, Y.; Bronstein, N.; Thompson, C.; Britt, D.; Salmeron, M.; Alivisatos, P.; Wang, L.-W. Hydroxylation of the Surface of PbS Nanocrystals Passivated with Oleic Acid. *Science (80-.).* **2014**, *344* (6190), 1380–1384.
(42) Niu, Z.; Peng, Q.; Gong, M.; Rong, H.; Li, Y. Oleylamine-Mediated Shape Evolution of Palladium Nanocrystals. *Angew. Chem. Int. Ed* **2011**, *50*, 6315–6319.
(43) Yang, Z.; Klabunde, K. J. Synthesis of Nearly Monodisperse Palladium (Pd) Nanoparticles by Using Oleylamine and Trioctylphosphine Mixed Ligands. *J. Organomet. Chem.* **2009**, *694*, 1016–1021.
(44) Liu, P.; Qin, R.; Fu, G.; Zheng, N. Surface Coordination Chemistry of Metal Nanomaterials. *J. Am. Chem. Soc.* **2017**, *139*, 2122–2131.
(45) Langille, M. R.; Personick, M. L.; Zhang, J.; Mirkin, C. A. Defining Rules for the Shape Evolution of Gold Nanoparticles. *J. Am. Chem. Soc.* **2012**, *134*, 14542–14554.
(46) Moulder, J. F.; Stickle, W. F.; Sobol, P. E.; Bomben, K. D. *Handbook of X-Ray Photoelectron Spectroscopy*; Chastain, J., Ed.; Perkin-Elmer Corporation Physical Electronics Division: Minnesota, 1992.
(47) Bolzfin, A. E. Phenomenological Aspects Related to the Electrochemical Behaviour of Smooth

Palladium Electrodes in Alkaline Solutions. *J. Electroanal. Chem.* **1995**, *380*, 127–138.
(48) Ghosh, S.; Remita, H.; Kar, P.; Choudhury, S.; Sardar, S.; Beaunier, P.; Roy, P. S.; Bhattacharya, S. K.; Pal, S. K. Facile Synthesis of Pd Nanostructures in Hexagonal Mesophases as a Promising Electrocatalyst for Ethanol Oxidation. *J. Mater. Chem. A* **2015**, *3*, 9517–9527.
(49) Zhao, Y.; Li, X.; Schechter, J. M.; Yang, Y. Revisiting the Oxidation Peak in the Cathodic Scan of the Cyclic Voltammogram of Alcohol Oxidation on Noble Metal Electrodes. *RSC Adv.* **2016**, *6*, 5384–5390.
(50) Huang, W.; Ma, X.; Wang, H.; Feng, R.; Zhou, J.; Duchesne, P. N.; Zhang, P.; Chen, F.; Han, N.; Zhao, F.; et al. Promoting Effect of Ni(OH)2 on Palladium Nanocrystals Leads to Greatly Improved Operation Durability for Electrocatalytic Ethanol Oxidation in Alkaline Solution. *Adv. Mater.* **2017**, *29*, 1703057.
(51) Jiang, F.; Yao, Z.; Yue, R.; Du, Y.; Xu, J.; Yang, P.; Wang, C. Electrochemical Fabrication of Long-Term Stable Pt-Loaded PEDOT/Graphene Composites for Ethanol Electrooxidation. *Int. J. Hydrogen Energy* **2012**, *37*, 14085–14093.
(52) Xin, H. L.; Mundy, J. A.; Liu, Z.; Cabezas, R.; Hovden, R.; Kourkoutis, L. F.; Zhang, J.; Subramanian, N. P.; Makharia, R.; Wagner, F. T.; et al. Atomic-Resolution Spectroscopic Imaging of Ensembles of Nanocatalyst Particles Across the Life of a Fuel Cell. *Nano Lett.* **2012**, *12*, 490–497.
(53) Monyoncho, E. A.; Steinmann, S. N.; Michel, C.; Baranova, E. A.; Woo, T. K.; Sautet, P. Ethanol Electro-Oxidation on Palladium Revisited Using Polarization Modulation Infrared Reflection Absorption Spectroscopy (PM-IRRAS) and Density Functional Theory (DFT): Why Is It Difficult To Break the C−C Bond? *ACS Catal.* **2016**, *6*, 4894–4906.
(54) Wu, Z.; Miao, B.; Hopkins, E.; Park, K.; Chen, Y.; Jiang, H.; Zhang, M.; Zhong, C.; Wang, L. Poisonous Species in Complete Ethanol Oxidation Reaction on Palladium Catalysts. *J. Phys. Chem. C* **2019**, *123*, 20853–20868.
(55) Gunji, T.; Noh, S. H.; Tanabe, T.; Han, B.; Nien, C. Y.; Ohsaka, T.; Matsumoto, F. Enhanced Electrocatalytic Activity of Carbon-Supported Ordered Intermetallic Palladium-Lead (Pd3Pb) Nanoparticles toward Electrooxidation of Formic Acid. *Chem. Mater.* **2017**, *29*, 2906–2913.
(56) Nafria, R.; Genç, A.; Ibáñez, M.; Arbiol, J.; Ramírez de la Piscina, P.; Homs, N.; Cabot, A. Co−Cu Nanoparticles: Synthesis by Galvanic Replacement and Phase Rearrangement during Catalytic Activation. *Langmuir* **2016**, *32*, 2267–2276.